Grid-following Converter Dynamics under Large Sub-synchronous Voltage Fluctuations

Benedikt Grüger, Florian Steinke
Energy Information Networks & Systems Lab
Technical University of Darmstadt
Darmstadt, Germany
benedikt.grueger@eins.tu-darmstadt.de

Adeel Jamal, Gerd Griepentrog
Institute of Power Electronics and Control of Drives
Technical University of Darmstadt
Darmstadt, Germany
adeeljamal@ieee.org

***Abstract*—The growing integration of converter-interfaced power sources into distribution grids leads to novel dynamic stability concerns. This paper investigates the stability of a grid-following converter under large sub-synchronous square-wave modulations of the grid voltage amplitude. By modelling only the critical dynamical processes of the converter control architecture, specifically direct voltage control and the phase-locked loop, we arrive at a non-linear fourth-order differential-algebraic system. Under these voltage disturbances, we study the influence of grid strength and the damping of the phase-locked loop on system behaviour. Our results show that the dynamic response is much stronger than predicted by small-signal analysis. For extreme grid conditions, we identify an instability associated with the converter's loss of synchronisation. This study provides insights into the non-linear dynamic behaviour of grid-following converters under abnormal voltage profiles, plausibly induced by equipment malfunction or load altering attacks.**

***Index Terms*—dynamical systems, large signal stability, converter control, phase-locked loop**

I. Introduction

Grid-following converters, commonly employed in the context of, e.g., PV plants, are designed for reliable injection of DC power into an AC distribution grid. Given their growing overall number, "converter stability" constitutes a topic of utmost importance, which is why ENTSO-E mentions it as a novel element in the list of key stability concepts [1]. Lately, several examples of destabilizing process couplings in converter-dominated grids [2], [3] demonstrate the need for further research on dynamical behaviour of converters.

Stable converter operation depends on reliable voltage phase detection which is done by its synchronisation mechanism. The synchronous reference frame phase-locked loop (SRF-PLL; here, simply PLL) aligns an internal phase variable with the voltage phase measured at the converter's terminal [4], [5]. Since the other controllers' inputs are Park-transformed dq-quantities, which depend on the PLL's phase, robust phase detection, irrespective of voltage perturbations, is important for the entire converter control. Consequently, the design of such synchronization mechanisms remains a significant and ongoing area of research.

This work was sponsored by the German Federal Ministry of Education and Research in the project CyberStress, funding no. 13N16626. Moreover, it has been performed in the context of the LOEWE center emergenCITY [LOEWE/1/12/519/03/05.001(0016)/72].

Distortions in the local voltage profile can arise from different sources. Under weak grid conditions, the converter's power infeed modifies the local voltage, potentially compromising system stability [6]. Successful phase detection can also be hindered by voltage distortions caused by short-circuits, equipment malfunction, or non-linear loads [4]. Particularly large distortions can originate from, e.g., inrush-currents of large machines or synchronised load variations which, given the growing number of IoT devices and cyber-risks, might be intentionally caused in so-called load altering attacks [7]–[9].

Converter' transient behaviour is often assessed with small-signal methods based on linearisation of the model's differential equations [10], [11]; during major incidents like short-circuits, line drops, or large voltage jumps, however, non-linearities are not negligible. In recent years, concepts from dynamical systems theory have proven valuable in enhancing the understanding of large-signal behaviour of power converters [12]. As such, PLL parameter tuning that accounts for stability under large-signal perturbations was proposed [13]. Also, the phenomenon of sustained oscillations in converters was investigated using the Poincaré method and bifurcation theory [14]. Furthermore, the phase portrait method was employed to study loss of synchronism (LoS) in converters [13], [15], [16]. Related studies often focused on converter stability under voltage sags; however, the response to sequential large voltage variations, which can keep the converter in a permanent state of transition, has received little attention yet. In this scenario, cumulative effects may result in an overall amplified impact.

This work studies the dynamic response of a grid-following converter subjected to large, periodic voltage amplitude fluctuations. We specifically examine slow, i.e., sub-synchronous, oscillations that could, e.g., be generated by synchronised load switching in the distribution grid. For this, we employ a reduced order model, the extended generalised swing model (EGSM) [17], which explicitly models the dynamics of slow processes inside the converter and its control system, i.e., the direct voltage controller (DVC), and the DC-side capacitor, and the slow PLL.

Comparing the results of the small-signal approach to our integration-based analysis, we analyse the impact of non-linear mechanisms in this periodically perturbed converter system.

The present work is organised as follows: Our modelling

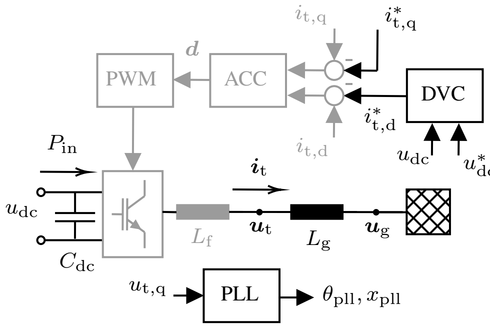

Fig. 1: Grid-following converter model given by Eq. (5): PLL, DVC, and DC capacitor dynamics are modelled explicitly while components coloured in grey are neglected or approximated.

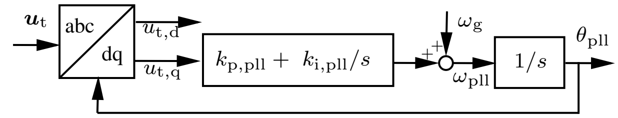

Fig. 2: Block diagram of Park transform and PLL: The voltage phase information is extracted from the q-component of the terminal voltage.

approach is presented in section II, based on which section III showcases the model's behaviour under voltage fluctuations and studies the influence of non-linearities on the system response. Finally, section IV summarises the main findings and provides an outlook.

II. Modelling approach

This section introduces the model of a three-phase grid-following converter connected to an infinite AC bus that experiences periodic three-phase voltage amplitude fluctuations. Fig. 1 shows a typical control architecture of a grid-following converter comprising a PLL, DVC, and alternating current control (ACC) [6]. However, only processes with dynamical time scales comparable to the sub-synchronous voltage variations are modelled explicitly following a time-scale separation approach. These are the PLL and the DVC, both with bandwidths ranging between 10 and 100 Hz [18]. The faster ACC with 200 Hz, filter and power line dynamics, and pulse-width modulation (PWM) are approximated by algebraic relations and slower power in-feed dynamics are treated as constants. For a more detailed discussion on these assumptions in dynamical converter models see [15], [17]–[19].

In what follows, calligraphic letters represent matrices, while vector quantities are denoted using boldface characters. Throughout this study, three-phase signals are represented in (power-invariant) dq-frame with grid voltage angle reference $\theta_{\rm pll} \in \mathbb{R}$.

A. Converter Model

The AC power grid is represented by an infinite bus with constant angular grid frequency $\omega_{\rm g} \in \mathbb{R}_{\geq 0}$ and an impedance following a Thévenin modelling approach. Given the inductance $L_{\rm g} \in \mathbb{R}_{\geq 0}$ and zero grid resistance, the terminal voltage is

$$\boldsymbol{u}_{\rm t} = \boldsymbol{u}_{\rm g} + L_{\rm g}\omega_{\rm g} \begin{pmatrix} 0 & -1 \\ 1 & 0 \end{pmatrix} \boldsymbol{i}_{\rm t} = \begin{pmatrix} u_{\rm t,d} \\ u_{\rm t,q} \end{pmatrix} \in \mathbb{R}^2. \tag{1}$$

which depends on the terminal current $\boldsymbol{i}_{\rm t} = (i_{\rm t,d} \;\; i_{\rm t,q})^{\rm T}$ [20].

Given the phase mismatch $\varphi = \theta_{\rm pll} - \omega_g t \in [-\pi, \pi)$ at time $t \in \mathbb{R}$, denoted as *PLL phase* [21], the grid voltage is $\boldsymbol{u}_g = (u_{\rm g}\cos(\varphi) \;\; -u_{\rm g}\sin(\varphi))^{\rm T} \in \mathbb{R}^2$ where $u_{\rm g} \in \mathbb{R}_{\geq 0}$ is the (phase-to-phase) grid voltage amplitude.

The PLL shown in Fig. 2 tries to synchronise its internal phase variable $\theta_{\rm pll} \in [-\pi, \pi)$ to the phase of the terminal voltage by nullifying the q-component of the voltage via a PI controller [4], [5]. Its control parameters $k_{\rm p,pll}$, $k_{\rm i,pll} \in \mathbb{R}$ together define a damping ratio and a natural frequency [22], [23]

$$\zeta = \frac{k_{\rm p,pll}}{2}\sqrt{U_{\rm g}/k_{\rm i,pll}} \tag{2}$$

$$\omega_{\rm n} = \sqrt{k_{\rm i,pll}U_{\rm g}} \tag{3}$$

which also depends on nominal voltage amplitude $U_{\rm g} \in \mathbb{R}_{>0}$ [24], [25]. $\zeta = 1/\sqrt{2}$ constitutes a trade-off between small overshoots and fast response [22], [23]. The PLL has a resonance at frequency

$$f_{\rm res} = \frac{\omega_{\rm n}}{2\pi}\sqrt{1-\zeta^2} \tag{4}$$

if $\zeta < 1$. Low damping creates large overshoots which jeopardizes transient stability [6].

The DVC is implemented as a PI controller with control gains $k_{\rm p,dvc}, k_{\rm i,dvc} \in \mathbb{R}_{>0}$. It brings the DC voltage $u_{\rm dc} \in \mathbb{R}$ to its reference value $u^*_{\rm dc} \in \mathbb{R}$ through varying the d-component of the terminal current set-point $i^*_{\rm t,d} \in \mathbb{R}$. That way, active power balance is achieved at the capacitor, i.e., the power generated on the DC side $P_{\rm in} \in \mathbb{R}_{>0}$ equals the power fed into the AC grid $P_{\rm e} \coloneqq i_{\rm t,d}u_{\rm t,d} + i_{\rm t,q}u_{\rm t,q}$. The q-component of the terminal current set-point $i^*_{\rm q,t} \in \mathbb{R}$ is kept constant.

From the terminal current set-points, the ACC calculates a duty cycle signal $\boldsymbol{d} \in [0,1]^2$ which then is translated into switching action by the PWM which we do not model explicitly. Also, neglecting signal processing delays and (fast) ACC and filter dynamics, we assume $i_{\rm t,d} = i^*_{\rm t,d}$ and $i_{\rm t,q} = i^*_{\rm t,q}$ [26], [27].

All in all, this leads to a fourth-order converter model, the EGSM, with state $\boldsymbol{x} = (\varphi \;\; x_{\rm pll} \;\; u_{\rm dc} \;\; x_{\rm dvc})^{\rm T} \in \mathcal{C}$ and corresponding state space $\mathcal{C} \coloneqq [-\pi, \pi) \times \mathbb{R}^3$ [17]. Dynamics are described by a system of differential equation

$$\dot{\boldsymbol{x}} = \begin{pmatrix} \dot\varphi \\ \dot x_{\rm pll} \\ \dot u_{\rm dc} \\ \dot x_{\rm dvc} \end{pmatrix} = \begin{pmatrix} x_{\rm pll} + k_{\rm p,pll}u_{\rm t,q}, \\ k_{\rm i,pll}u_{\rm t,q}, \\ \frac{1}{C_{\rm dc}u_{\rm dc}}\left(P_{\rm in} - P_{\rm e}\right), \\ k_{\rm i,dvc}\left(u_{\rm dc} - u^*_{\rm dc}\right) \end{pmatrix} =: \boldsymbol{f}(\boldsymbol{x}; u_{\rm g}) \tag{5a}$$

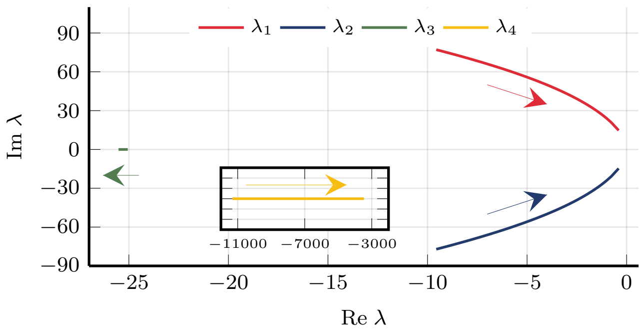

Fig. 3: Eigenvalues λ_i ($i \in \{1, \ldots, 4\}$) of the system Jacobian at $\boldsymbol{x}^{\mathrm{eq}}$ for different values $u_{\mathrm{g}} \in [0.63\,U_{\mathrm{g}}, 1.5\,U_{\mathrm{g}}]$: As u_{g} decreases, λ_1 and λ_2 approach the imaginary axis. Other parameters are $\zeta = 0.1$ and $L_{\mathrm{g}} = 10\,\mathrm{mH}$.

and corresponding algebraic relations

$$\begin{cases} i^*_{\mathrm{t,d}} &= k_{p,\mathrm{dvc}}\,(u_{\mathrm{dc}} - u^*_{\mathrm{dc}}) + x_{\mathrm{dvc}} \\ u_{\mathrm{t,d}} &= u_{\mathrm{g}} \cos\varphi - L_{\mathrm{g}}\omega_{\mathrm{g}} i^*_{t,q} \\ u_{\mathrm{t,q}} &= L_{\mathrm{g}}\omega_{\mathrm{g}} i^*_{\mathrm{t,d}} - u_{\mathrm{g}} \sin\varphi \\ P_{\mathrm{e}} &= u_{\mathrm{t,d}}\, i^*_{\mathrm{t,d}} + u_{\mathrm{t,q}}\, i^*_{\mathrm{t,q}}. \end{cases} \tag{5b}$$

For some parameter combinations, this model exhibits a (stable) equilibrium state $\boldsymbol{x}^{\mathrm{eq}} = (\varphi^{\mathrm{eq}} \;\; 0 \;\; u^*_{\mathrm{dc}} \;\; x^{\mathrm{eq}}_{\mathrm{dvc}})^{\mathrm{T}}$ derived in App. A.

Note that, in contrast to the original formulation of the EGSM, Eq. (5b) has $u_{\mathrm{t,d}} = U_g$ assuming instantaneous terminal voltage control [17]. Since we consider a purely grid-following control, terminal voltage in our model remains unregulated, i.e., $u_{t,d}$ is given by Eq. (1).

B. Grid Voltage fluctuations

We proceed with the mathematical formulation of the square-wave voltage amplitude fluctuations imposed on the converter. The external power grid is considered as operating in one of two discrete *grid states*, 1 and 2, corresponding to over- and under–voltage, respectively. Given $u_{\mathrm{g},0} \in \mathbb{R}$, frequency $f_{\mathrm{d}} \in \mathbb{R}_{>0}$, and amplitude $A_{\mathrm{d}} \in \mathbb{R}_{>0}$, the correspondingly fluctuating grid voltage amplitude is

$$u_{\mathrm{g}}(t) = u_{\mathrm{g},0} + A_{\mathrm{d}} \cdot p_\infty(t; f_{\mathrm{d}}) \in \{u_{\mathrm{g},1}, u_{\mathrm{g},2}\}, \tag{6}$$

where $p_\infty(t; f_{\mathrm{d}}) \in \{-1, 1\}$ is the square wave function. Given a cut-off $k_{\max} \in \mathbb{N}_{\geq 1}$, $p_\infty(t; f_{\mathrm{d}})$ can be approximated as

$$p_{k_{\max}}(t; f_d) = \frac{4}{\pi} \sum_{k=1,3,5,\ldots}^{k_{\max}} \frac{1}{k} \sin\left(2\pi f_{\mathrm{d}}\, kt\right), \tag{7}$$

summing over spectral components associated with odd harmonics. In the limit $k_{\max} \to \infty$, this yields the square wave.

In sum, the voltage fluctuations constitute an external driving of the converter system; accordingly, A_{d} is referred to as the driving amplitude, and f_{d} as the driving frequency.

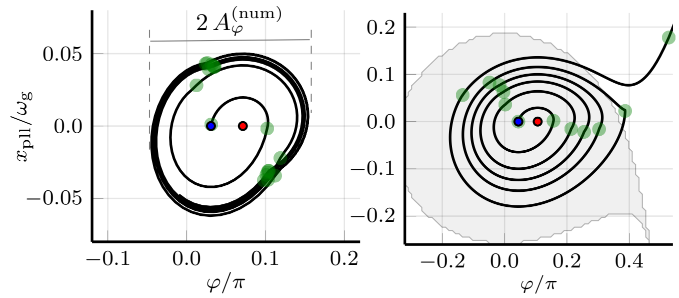

(a) $L_g = 7\,\mathrm{mH}$ (b) $L_g = 10\,\mathrm{mH}$

Fig. 4: System trajectory under grid voltage fluctuations shown in the reduced state space spanned by $(\varphi, x_{\mathrm{pll}})$: The equilibrium states $\boldsymbol{x}^{\mathrm{eq}}_1, \boldsymbol{x}^{\mathrm{eq}}_2$ are visualised as blue and red points, respectively. Green circles indicate grid state transitions. The simulation parameters are $\zeta = 0.1$ and $f_{\mathrm{d}} = 8.5\,\mathrm{Hz}$. In (b), a grey area indicates the basin of attraction (see App. B).

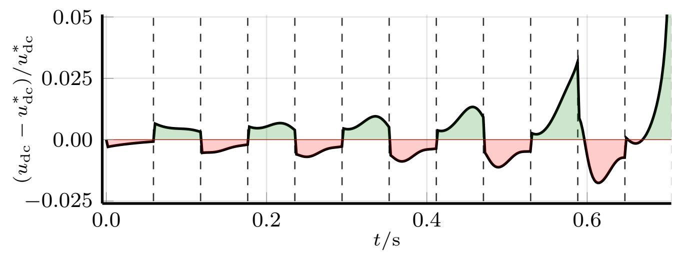

Fig. 5: Asymmetric oscillations of u_{dc} in unstable situation from Fig. 4b: Areas with positive (green) and negative (red) control error have different size. Grid state transitions are marked by vertical black dashed lines. The simulation parameters are $\zeta = 0.1$ and $f_{\mathrm{d}} = 8.5\,\mathrm{Hz}$, and $L_g = 10\,\mathrm{mH}$.

III. Simulation Analysis

Before showcasing the system behaviour, we discuss the simulation framework. Simulations are written in *Julia Programming Language* [28] employing the `DifferentialEquations.jl` package [29] with integration method “Tsit5” [30]. To better capture the discontinuities in u_{g} during integration, we select small evaluation time steps $\Delta t = 1/(2 f_{\mathrm{d}} \cdot 400)$.

The DVC has gain values $k_{\mathrm{p,dvc}} = 2$ and $k_{\mathrm{i,dvc}} = 50$. Furthermore, we choose DC-side voltage reference value $u^*_{\mathrm{dc}} = 700\,\mathrm{V}$ and capacitance $C_{\mathrm{dc}} = 150\,\mu\mathrm{F}$. The DC power source constantly provides $P_{\mathrm{in}} = 10\,\mathrm{kW}$ while $i^*_{\mathrm{t,q}} = 0$. PLL parameters are selected in terms of damping $\zeta \in [0.05, 0.4]$ and resonance frequency which is kept at $f_{\mathrm{res}} = 10\,\mathrm{Hz}$ (see Eqs. (2) and (4)). The grid has frequency $\omega_{\mathrm{g}} = 2\pi \cdot 50\,\mathrm{Hz}$ and nominal voltage $U_{\mathrm{g}} = \sqrt{3} \cdot 230\,\mathrm{V}$. Different grid strengths are considered corresponding to short-circuit ratios between 5 and 51: $L_{\mathrm{g}} \in \{1\,\mathrm{mH}, 4\,\mathrm{mH}\}$ representing a strong and $L_{\mathrm{g}} \in \{7\,\mathrm{mH}, 10\,\mathrm{mH}\}$ representing a weak grid.

The fluctuations of the grid voltage amplitude are modelled with the square wave function in Eq. (7) employing $u_{\mathrm{g},0} = U_{\mathrm{g}}$, $A_{\mathrm{d}} = 0.2\,U_{\mathrm{g}}$, and $f_{\mathrm{d}} \in [0.5, 30]\,\mathrm{Hz}$.

$$\nabla_{\boldsymbol{x}} \boldsymbol{f}(\boldsymbol{x}; u_{\mathrm{g}}) = \begin{pmatrix} -u_{\mathrm{g}} k_{\mathrm{p,pll}} \cos\varphi & 1 & k_{\mathrm{p,pll}} \omega_{\mathrm{g}} L_{\mathrm{g}} k_{\mathrm{p,dvc}} & k_{\mathrm{p,pll}} \omega_{\mathrm{g}} L_{\mathrm{g}} \\ -u_{\mathrm{g}} k_{\mathrm{i,pll}} \cos\varphi & 0 & k_{\mathrm{i,pll}} \omega_{\mathrm{g}} L_{\mathrm{g}} k_{\mathrm{p,dvc}} & k_{\mathrm{i,pll}} \omega_{\mathrm{g}} L_{\mathrm{g}} \\ \frac{u_{\mathrm{g}}}{C_{\mathrm{dc}} u_{\mathrm{dc}}} \sin\varphi \, i^*_{\mathrm{t,d}} & 0 & -\frac{1}{C_{\mathrm{dc}} u^2_{\mathrm{dc}}} (P_{\mathrm{in}} - P_{\mathrm{e}}) - \frac{u_{\mathrm{t,d}} k_{\mathrm{p,dvc}}}{C_{\mathrm{dc}} u_{\mathrm{dc}}} & -\frac{u_{\mathrm{t,d}}}{C_{\mathrm{dc}} u_{\mathrm{dc}}} \\ 0 & 0 & k_{\mathrm{i,dvc}} & 0 \end{pmatrix} \tag{8}$$

A. Transient dynamics

We study system behaviour under fluctuating grid voltage amplitude, for particularly low damping $\zeta = 0.1$ and high inductances $L_{\mathrm{g}} \in \{7, 10\}$ mH.

One prerequisite for transient stability is the existence of a post-fault equilibrium. In our case, this means that each grid voltage amplitude, $u_{\mathrm{g},1} = 1.2\,U_{\mathrm{g}}$ and $u_{\mathrm{g},2} = 0.8\,U_{\mathrm{g}}$, there must exist a corresponding equilibrium $\boldsymbol{x}_1^{\mathrm{eq}}, \boldsymbol{x}_2^{\mathrm{eq}} \in \mathbb{R}^4$, respectively. We here show that this is the case for $L_{\mathrm{g}} = 10\,\mathrm{mH}$ and holds true also for smaller inductances L_{g}. Shown in Fig. 3, the root-loci of the Jacobian's eigenvalues (see Eq. (8)) for $u_{\mathrm{g}} \in [0.63\,U_{\mathrm{g}}, 1.5\,U_{\mathrm{g}}]$ indicate small-signal stability of the equilibrium. For $u_{\mathrm{g}} < \sqrt{2\omega_{\mathrm{g}} L_{\mathrm{g}} P_{\mathrm{in}}} \approx 0.63\,U_{\mathrm{g}}$, the equilibrium ceases to exist (compare App. A). This lower bound for the voltages decreases with smaller L_{g}; hence, the equilibria $\boldsymbol{x}_1^{\mathrm{eq}}, \boldsymbol{x}_2^{\mathrm{eq}}$ also exist for higher grid strengths.

Having checked for existing equilibria, we proceed with the assessment of the system dynamics. Initialising with $\boldsymbol{x}(t=0) = \boldsymbol{x}_1^{\mathrm{eq}}$, we integrate Eq. (5) up to $T = 5\,\mathrm{s}$ varying the voltage amplitude in Eq. (6) with $f_{\mathrm{d}} = 8.5\,\mathrm{Hz}$. The system shows two different kinds of long-term behaviour. For $L_{\mathrm{g}} = 7\,\mathrm{mH}$, the dynamics shown in Fig. 4a are stable in the sense that, after a transient lasting several driving periods, the converter state settles down onto a constant orbit. By contrast, at higher grid impedance, $L_{\mathrm{g}} = 10\,\mathrm{mH}$, the driving renders the system unstable. After several switching periods, the trajectory shown in Fig. 4b leaves the system's basin of stability (see App. B).

The unstable dynamics are accompanied by growing state variables oscillations. Fig. 5 shows them for the DC voltage u_{dc}. Since the oscillations are asymmetric in the sense that green and red areas in the Figure differ, the DVC's integral state grows with each driving period presumably causing the observed converter instability.

B. PLL Phase Response Magnitude

For most parameter combinations, dynamics end up on a stable steady-state oscillation where each state variable oscillates with some amplitude. In the following, we employ small-signal analysis and numerical integration to study the impact of damping ζ and grid inductance L_{g} on the response magnitude of the PLL phase for different driving frequencies $f_{\mathrm{d}} \in [0.5, 30.0]\,\mathrm{Hz}$.

For the small signal analysis, we derive the system's transfer function. Subjected to deviations of the grid voltage amplitude

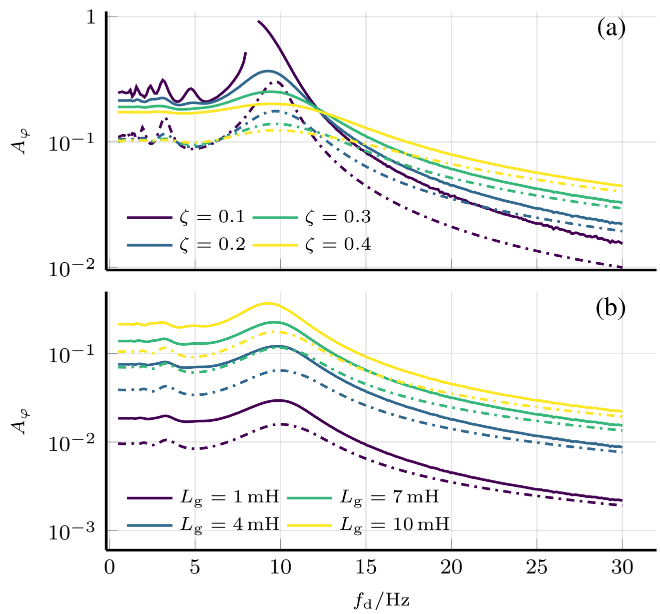

Fig. 6: PLL phase response magnitude to grid voltage amplitude fluctuations: Response curves obtained from integration, $A_\varphi^{(\mathrm{num})}$ (solid), and from small-signal analysis, $A_\varphi^{(\mathrm{lin})}$ (dashed), are shown for (a) $L_{\mathrm{g}} = 10\,\mathrm{mH}$ and different ζ, and (b) $\zeta = 0.2$ and different L_{g}. Each curve is calculated at 250 equally spaced values of the driving frequency $f_{\mathrm{d}} \in [0.5, 30]\,\mathrm{Hz}$ in Eq. (6). In case of unstable dynamics, no data points are plotted.

$\delta u_{\mathrm{g}} = u_{\mathrm{g}} - u_{\mathrm{g},0}$, the system dynamics close to the corresponding equilibrium $\boldsymbol{x}_0^{\mathrm{eq}} \in \mathbb{R}^4$ can be approximated as

$$\delta\dot{\boldsymbol{x}} = \nabla_{\boldsymbol{x}} \boldsymbol{f}\left(\boldsymbol{x}_0^{\mathrm{eq}}; u_{\mathrm{g}}\right) \delta\boldsymbol{x} + \nabla_{u_{\mathrm{g}}} \boldsymbol{f}\left(\boldsymbol{x}_0^{\mathrm{eq}}; u_{\mathrm{g}}\right) \delta u_{\mathrm{g}} \tag{9}$$

where deviations $\delta\boldsymbol{x} = \boldsymbol{x} - \boldsymbol{x}_0^{\mathrm{eq}} \in \mathbb{R}^N$. The Jacobian $\nabla_{\boldsymbol{x}} \boldsymbol{f}(\boldsymbol{x}; u_{\mathrm{g}})$ is given in Eq. (8) for $i^*_{\mathrm{t,q}} = 0$; furthermore, the gradient

$$\nabla_{u_{\mathrm{g}}} \boldsymbol{f}\left(\boldsymbol{x}; u_{\mathrm{g}}\right) = \begin{pmatrix} -k_{\mathrm{p,pll}} \sin\varphi \\ -k_{\mathrm{i,pll}} \sin\varphi \\ -\frac{1}{C_{\mathrm{dc}} u_{\mathrm{dc}}} \cos\varphi \, i^*_{\mathrm{t,d}} \\ 0 \end{pmatrix}$$

quantifies the state's sensitivity to changes in grid voltage amplitude. Taking the Laplace transform of Eq. (9) and rearranging terms yields the transfer function

$$\boldsymbol{h}(s) = \delta\hat{\boldsymbol{x}}(s)/\delta\hat{u}_{\mathrm{g}}(s) = \left(s\mathbb{1} - \nabla_{\boldsymbol{x}} \boldsymbol{f}\right)^{-1} \nabla_{u_{\mathrm{g}}} \boldsymbol{f} \in \mathbb{C}^4 \tag{10}$$

for $s = \mathrm{j}\omega \in \mathbb{C}$, j the imaginary unit, and $\mathbb{1} \in \mathbb{R}^{N\times N}$ the identity matrix. Then, the linear response to varying voltage amplitude in Eq. (7) is the superposition of response to spectral components $\hat{u}_\mathrm{g}(\mathrm{j}2\pi f_\mathrm{d}k) = 4A_\mathrm{d}/(\pi \cdot k)$ for $k \in \{1, 3, 5, \ldots, k_\mathrm{max}\}$. Transformed back to time domain, the response magnitude of the PLL phase is

$$A_\varphi^{(\mathrm{lin})} = \max_t \sum_{k=1,3,5,\ldots}^{k_\mathrm{max}} \frac{4A_\mathrm{d}}{\pi} \frac{a_k}{k} \sin(2\pi f_\mathrm{d} k t + \theta_k) \qquad (11)$$

where $a_k = |h_1(\mathrm{j}2\pi f_\mathrm{d} k)|$ and $\theta_k = \arg(h_1(\mathrm{j}2\pi f_\mathrm{d} k))$. In our analysis, we take $k_\mathrm{max} = 101$.

Second, we determine the response numerically by integrating the system dynamics up to time $T = 4\,\mathrm{s}$. After the trajectory $\boldsymbol{x}(t)$ has settled down on a steady-state oscillation, the PLL phase response magnitude is quantified by

$$A_\varphi^{(\mathrm{num})} = \left(\max_t \varphi(t) - \min_t \varphi(t)\right) \Big/ 2 \qquad (12)$$

for $t \in [T, T + 2\,\mathrm{s}]$. If the system does not show stable long-term behaviour the response is considered undefined.

The results are illustrated in Fig. 6. If driving happens sufficiently slowly the system can relax to the respective equilibrium point within half a driving period, i.e., $\boldsymbol{x} \to \boldsymbol{x}_1^\mathrm{eq}$ or $\boldsymbol{x}_2^\mathrm{eq}$. As a consequence, the PLL phase response is determined by the overshoots of the individual relaxation dynamics [31, p. 285]. For $f_\mathrm{d} \to \infty$, the PLL acts as a low-pass filter such that the response shrinks to zero.

In the resonance regime, the PLL phase response curve has several maxima the largest of which matches with the PLL resonance frequency $f_\mathrm{res} = 10\,\mathrm{Hz}$ from Eq. (4). Other (smaller) maxima are supposedly triggered by higher spectral components of the driving function in Eq. (7) and/or originate from sub-harmonic resonance.

Fig. 6a illustrates the destabilising effect of low damping. Upon decreasing ζ, the resonance maxima grow in magnitude. For $\zeta = 0.1$ and $L = 10\,\mathrm{mH}$, dynamics are unstable at driving frequencies slightly smaller than f_res. Similar to the case shown earlier in Fig. 4b, the perturbation leads to LoS.

Also, lower grid strength increases the PLL response. Shown in Fig. 6b, the grid inductance scales the overall PLL phase response where for larger L_g the resonance peak slightly moves to smaller frequencies.

Fig. 7 visualises the process couplings of the EGSM. The small-signal response $A_\varphi^{(\mathrm{lin})}$ systematically underestimates the actual system response $A_\varphi^{(\mathrm{num})}$. This is due to the to grid voltage u_g acting as a time-varying parameter in Eq. (5). The term $\sin\varphi\, u_\mathrm{g} \approx \varphi\, u_\mathrm{g}$ is of special relevance here. Generally, we have $\varphi(t) = \varphi_0 + \Delta\varphi(t)$ and $u_\mathrm{g}(t) = u_{\mathrm{g},0} + \Delta u_\mathrm{g}(t)$ for offsets $\varphi_0, u_{\mathrm{g},0} \in \mathbb{R}_{>0}$. Simplifying $\Delta\varphi(t) = A_\varphi \sin(\omega_\mathrm{d} t)$, $\Delta u_\mathrm{g}(t) = A_\mathrm{d} \sin(\omega_\mathrm{d} t + \alpha)$ and phase difference $\alpha \in (-\pi, \pi]$, this is

$$\begin{aligned}\varphi(t) u_\mathrm{g}(t) = \varphi_0 u_{\mathrm{g},0} + u_{\mathrm{g},0} A_\varphi \sin(\omega_\mathrm{d} t) + \varphi_0 A_\mathrm{d} \sin(\omega_\mathrm{d} t + \alpha) \\ + \frac{1}{2} A_\mathrm{d} A_\varphi \left(\cos(\alpha) - \cos(2\omega_\mathrm{d} t + \alpha)\right) \qquad (13)\end{aligned}$$

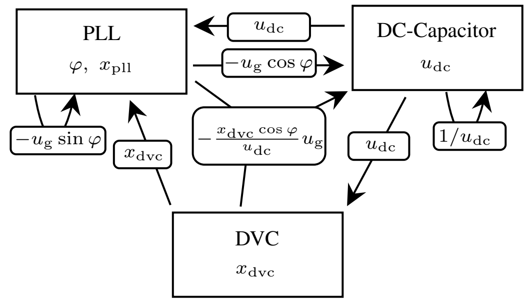

Fig. 7: Visualisation of process interactions for $i^*_{\mathrm{t,q}} = 0$: Coupling terms in Eq. (5) are represented by arrows. Constant factors are omitted.

where only terms in the first line of the r.h.s. in Eq. (13) are accounted for in the linear response in Eq. (10).

On the other hand, the small-signal approach does not account for the higher-order terms in the second line of Eq. (13). The term $-\cos(2\omega_\mathrm{d} t + \alpha)$ introduces an additional spectral component to the response, which entails an important role in the sub-harmonic resonance observed in Fig. 6. The term $\cos(\alpha)$, on the other hand, shifts the average value of the oscillation of $\varphi(t) \cdot u_\mathrm{g}(t)$. In the simulations, we observe that $\varphi(t)$ and $u_\mathrm{g}(t)$ tend to oscillate out of phase such that $\cos\alpha < 0$ (compare Fig. 4). This shift in the phase portrait towards larger PLL phases effectively leads to larger absolute values of the time-derivatives in Eq. (5) thereby amplifying the PLL phase response. This effect is associated with parametric resonance, to be examined in future studies.

IV. Conclusion

Sub-synchronous large voltage fluctuations pose a danger to converter stability. This paper examined the dynamic response of a grid-following converter to slow, large, periodic voltage amplitude fluctuations at the terminal for different controller settings and grid strengths. Employing a reduced-order model, we observe that the response is mainly shaped by the PLL resonance. A non-linearity amplifies the actual PLL phase response rendering the transfer function approach inappropriate for the quantitative analysis. If PLL damping is low, the voltage fluctuations can cause LoS.

More research is needed to understand the potential impact voltage amplitude fluctuations have on converter systems. For example, voltage amplitude variations are likely to be accompanied by phase jumps which has not been considered here. Then, the ability of protection schemes like current limits and PLL frequency-band limits, or stabilising controls like PLL freezing [6] to keep the converter stable in the considered scenarios should be studied. From this, novel design guidelines for stable control of grid-following converters can be derived.

Showcasing the limits of linear stability analysis of a grid-following converter in presence of a periodically changing voltage amplitude, this work contributes to ongoing converter modelling efforts. It emphasizes the importance of non-linear phenomena in externally driven converter systems, particularly relevant for assessing the risks posed by load-altering attacks.

Appendix

A. Fixed points of the EGSM

To find the fixed points of the EGSM, set the time derivatives of Eq. (5a) to zero. Accordingly, $P_{\mathrm{in}} = P_{\mathrm{e}}$ and $u_{\mathrm{t,q}} = 0$. Furthermore, states attain values $x_{\mathrm{pll}} = 0$, $u_{\mathrm{dc}} = u_{\mathrm{dc}}^*$, and the mutually dependent expressions

$$x_{\mathrm{dvc}} = \frac{P_{\mathrm{in}}}{u_{\mathrm{g}}\cos(\varphi)} \tag{A.1}$$

$$u_{\mathrm{g}}\sin\varphi = \frac{\omega_{\mathrm{g}} L_{\mathrm{g}} x_{\mathrm{dvc}}}{u_{\mathrm{g}}}. \tag{A.2}$$

for $i_{\mathrm{t,q}}^* = 0$. Eq. (A.1) and Eq. (A.2) together have two solutions. Plugging one equation into the other yields the stable fixed point, the equilibrium, $\boldsymbol{x}^{\mathrm{eq}}$ and the unstable fixed point $\boldsymbol{x}^{\mathrm{un}}$ which are

$$\boldsymbol{x}^{\mathrm{eq}} = (\varphi^{\mathrm{eq}} \;\; 0 \;\; u_{\mathrm{dc}}^* \;\; x_{\mathrm{dvc}}^{\mathrm{eq}})^{\mathrm{T}} \tag{A.3}$$

$$\boldsymbol{x}^{\mathrm{un}} = (\pi + \varphi^{\mathrm{eq}} \;\; 0 \;\; u_{\mathrm{dc}}^* \;\; -x_{\mathrm{dvc}}^{\mathrm{eq}})^{\mathrm{T}} \tag{A.4}$$

where $\varphi^{\mathrm{eq}} = \frac{1}{2}\mathrm{arcsin}\left(\frac{2\omega_{\mathrm{g}} L_{\mathrm{g}} P_{\mathrm{in}}}{u_{\mathrm{g}}^2}\right)$. If $2\omega_{\mathrm{g}} L_{\mathrm{g}} P_{\mathrm{in}} > u_{\mathrm{g}}^2$, the system has no fixed points.

B. Basin of stability

Given intervals $\mathcal{K}_\varphi \subset (-\pi, \pi]$ and $\mathcal{K}_{x_{\mathrm{pll}}} \subset \mathbb{R}$, the basin of stability of the EGSM is numerically obtained for the reduced phase space $\mathcal{K}_\varphi \times \mathcal{K}_{x_{\mathrm{pll}}}$. The system is evolved with Eq. 5 departing from different initial conditions $\boldsymbol{x}(t=0) = \boldsymbol{x}_0^{\mathrm{eq}} + \delta\tilde{\boldsymbol{x}}$ where deviations $\delta\tilde{\boldsymbol{x}} \in \{(\delta\tilde{\varphi} \;\; \delta\tilde{x}_{\mathrm{pll}} \;\; 0 \;\; 0)^{\mathrm{T}} | (\delta\tilde{\varphi}, \delta\tilde{x}_{\mathrm{pll}}) \in \mathcal{K}_\varphi \times \mathcal{K}_{x_{\mathrm{pll}}}\}$. The $\delta\tilde{\varphi}, \delta\tilde{x}_{\mathrm{pll}}$ are selected as distributed on a 80×80 - grid. We choose the tolerance $\varepsilon = 10^{-3}$. For $T = 50\,\mathrm{s}$, a system trajectory is considered converged if

$$||\boldsymbol{x}(T) - \boldsymbol{x}_0^{\mathrm{eq}}|| < \varepsilon\,;$$

otherwise, the system is classified as unstable.

References

[1] ENTSO-E, "Stability Management in Power Electronics Dominated Systems: A Prerequisite to the Success of the Energy Transition," ENTSO-E Position Paper, Jun. 2022.

[2] J. Enslin and P. Heskes, "Harmonic interaction between a large number of distributed power inverters and the distribution network," *IEEE Trans. Power Electron.*, vol. 19, no. 6, pp. 1586–1593, 2004.

[3] M. Lu, X. Wang, P. C. Loh, and F. Blaabjerg, "Resonance interaction of multiparallel grid-connected inverters with LCL filter," *IEEE Trans. Power Electron.*, vol. 32, no. 2, pp. 894–899, 2017.

[4] F. Blaabjerg, R. Teodorescu, M. Liserre, and A. Timbus, "Overview of Control and Grid Synchronization for Distributed Power Generation Systems," *IEEE Trans. Ind. Electron.*, vol. 53, no. 5, pp. 1398–1409, 2006.

[5] X.-Q. Guo, W.-Y. Wu, and H.-R. Gu, "Phase locked loop and synchronization methods for grid-interfaced converters: a review," *Przeglad Elektrotechniczny*, vol. 87, no. 4, pp. 182–187, 2011.

[6] X. Wang, M. G. Taul, H. Wu, Y. Liao, F. Blaabjerg, and L. Harnefors, "Grid-Synchronization Stability of Converter-Based Resources—An Overview," *IEEE Open J. Ind. Appl.*, vol. 1, pp. 115–134, 2020.

[7] A.-H. Mohsenian-Rad and A. Leon-Garcia, "Distributed Internet-Based Load Altering Attacks Against Smart Power Grids," *IEEE Trans. Smart Grid*, vol. 2, no. 4, pp. 667–674, 2011.

[8] S. Lakshminarayana, S. Adhikari, and C. Maple, "Analysis of IoT-Based Load Altering Attacks Against Power Grids Using the Theory of Second-Order Dynamical Systems," *IEEE Trans. Smart Grid*, vol. 12, no. 5, pp. 4415–4425, 2021.

[9] A. Jamal, B. Grüger, K. Kuroptev, M. Wolff, F. Steinke, and G. Griepentrog, "Exploring Cyber Threats based on Harmonic Distortions: A Testbed to analyze Attack Scenarios," in *Proc. IEEE ECCE*, 2024, pp. 1–6.

[10] R. Rosso, M. Andresen, S. Engelken, and M. Liserre, "Analysis of the Interaction Among Power Converters Through Their Synchronization Mechanism," *IEEE Trans. Power Electron.*, vol. 34, no. 12, pp. 12 321–12 332, 12 2019.

[11] U. Markovic, O. Stanojev, P. Aristidou, E. Vrettos, D. Callaway, and G. Hug, "Understanding Small-Signal Stability of Low-Inertia Systems," *IEEE Trans. Power Syst.*, vol. 36, no. 5, pp. 3997–4017, Sep. 2021.

[12] S. H. Strogatz, *Nonlinear Dynamics and Chaos: With Applications to Physics, Biology, Chemistry, and Engineering*, 2nd ed. Boca Raton: CRC Press, May 2019.

[13] Z. Ling, J. Xu, Y. Shi, Y. Qiao, and S. Xie, "Large-signal Stability Analysis and Parameter Optimization of Grid-tied Inverter Considering Phase-locked Loop Nonlinearity," in *Proc. IEEE PEAC*, 2022, pp. 577–582.

[14] R. Ma, Z. Yang, S. Cheng, and M. Zhan, "Sustained oscillations and bifurcations in three-phase voltage source converter tied to AC grid," *IET Renew. Power Gener.*, vol. 14, no. 18, pp. 3770–3781, 2020.

[15] X. He and H. Geng, "Synchronization Stability Analysis and Enhancement of Grid-Tied Multi-Converter Systems," in *IEEE-IAS Annu. Meet.*, 2020, pp. 1–8.

[16] Z. Yang, R. Ma, S. Cheng, and M. Zhan, "Nonlinear Modeling and Analysis of Grid-Connected Voltage-Source Converters Under Voltage Dips," *IEEE Journal of Emerging and Selected Topics in Power Electronics*, vol. 8, no. 4, pp. 3281–3292, 2020.

[17] R. Ma, Y. Zhang, Z. Yang, J. Kurths, M. Zhan, and C. Lin, "Synchronization stability of power-grid-tied converters," *Chaos*, vol. 33, no. 3, p. 032102, Mar. 2023.

[18] H. Yuan, X. Yuan, and J. Hu, "Modeling of Grid-Connected VSCs for Power System Small-Signal Stability Analysis in DC-Link Voltage Control Timescale," *IEEE Trans. Power Syst.*, vol. 32, no. 5, pp. 3981–3991, 2017.

[19] F. Dörfler and D. Groß, "Control of low-inertia power systems," *Annu. Rev. Control Robot. Auton. Syst.*, vol. 6, no. 6, pp. 415–445, May 2023.

[20] B. Wen, D. Boroyevich, R. Burgos, P. Mattavelli, and Z. Shen, "Analysis of D-Q Small-Signal Impedance of Grid-Tied Inverters," *IEEE Trans. Power Electron.*, vol. 31, no. 1, pp. 675–687, Jan. 2016.

[21] Q. Hu, L. Fu, F. Ma, and F. Ji, "Large Signal Synchronizing Instability of PLL-Based VSC Connected to Weak AC Grid," *IEEE Trans. Power Syst.*, vol. 34, no. 4, pp. 3220–3229, 2019.

[22] S.-K. Chung, "A phase tracking system for three phase utility interface inverters," *IEEE Trans. Power Electron.*, vol. 15, no. 3, May 2000.

[23] R. Teodorescu, M. Liserre, and P. Rodríguez, *Grid Converters for Photovoltaic and Wind Power Systems*, 1st ed. Chichester: Wiley-IEEE Press, 2011.

[24] B. Hammer, "Revisiting the Synchronous Reference Frame Phase-Locked Loop from a System Theory Point of View," in *ICCEP*, Jun. 2023, pp. 481–486.

[25] G. Escobar, L. Ibarra, J. E. Valdez-Resendiz, J. C. Mayo-Maldonado, and D. Guillen, "Nonlinear Stability Analysis of the Conventional SRF-PLL and Enhanced SRF-EPLL," *IEEE Access*, vol. 9, pp. 59 446–59 455, 2021.

[26] R. Ma, Q. Qiu, J. Kurths, and M. Zhan, "Fast-Slow-Scale Interaction Induced Parallel Resonance and its Suppression in Voltage Source Converters," *IEEE Access*, vol. 9, pp. 90 126–90 141, 2021.

[27] Z. Yang, J. Yu, J. Kurths, and M. Zhan, "Nonlinear Modeling of Multi-Converter Systems Within DC-Link Timescale," *IEEE J. Emerg. Sel. Top. Circuits Syst.*, vol. 11, no. 1, pp. 5–16, 2021.

[28] J. Bezanson, A. Edelman, S. Karpinski, and V. B. Shah, "Julia: A fresh approach to numerical computing," *SIAM Rev.*, vol. 59, no. 1, pp. 65–98, 2017.

[29] C. Rackauckas and Q. Nie, "DifferentialEquations.jl – A Performant and Feature-Rich Ecosystem for Solving Differential Equations in Julia," *J. Open Res. Softw.*, vol. 5, no. 1, 2017.

[30] C. Tsitouras, "Runge–Kutta pairs of order 5(4) satisfying only the first column simplifying assumption," *Comput. Math. Appl.*, vol. 62, no. 2, pp. 770–775, 2011.

[31] R. C. Dorf and R. H. Bishop, *Modern Control Systems: International Edition*, 11st ed. Upper Saddle River, N.J: Pearson, 2008.